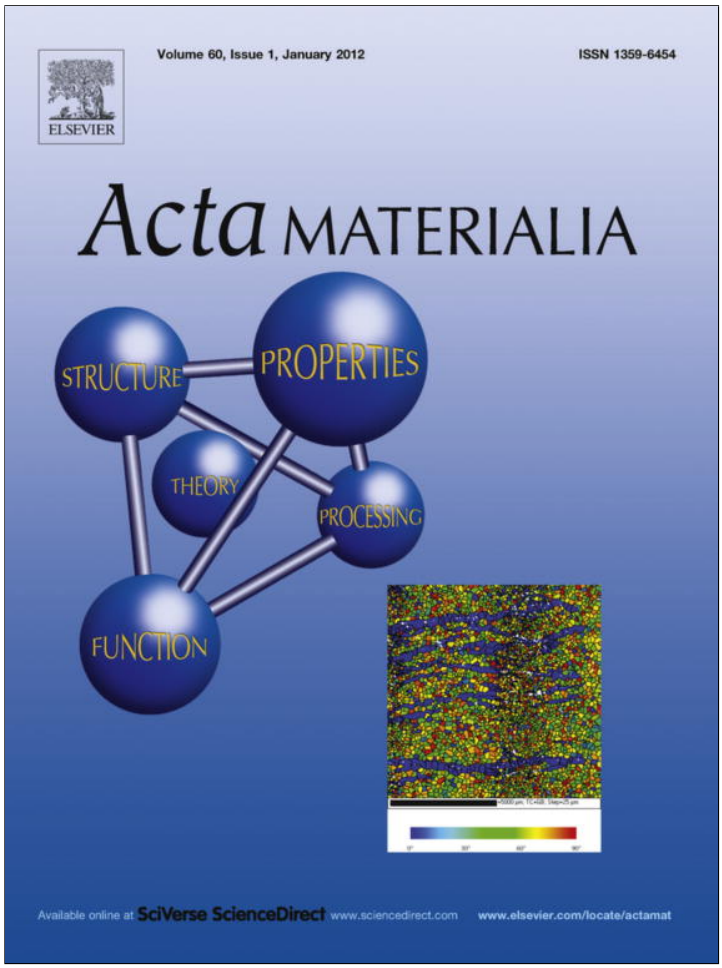

(This is a sample cover image for this issue. The actual cover is not yet available at this time.)

Available online at www.sciencedirect.com

SciVerse ScienceDirect

Acta Materialia 60 (2012) 3840–3848

Acta MATERIALIA

www.elsevier.com/locate/actamat

Competition of the primary and peritectic phases in hypoperitectic Cu–Sn alloys solidified at low speed in a diffusive regime

J. Valloton *, J.-D. Wagnière, M. Rappaz

Computational Materials Laboratory, Institute of Materials, Ecole Polytechnique Fédérale de Lausanne, Station 12, CH-1015 Lausanne, Switzerland

Received 18 November 2011; received in revised form 5 March 2012; accepted 17 March 2012

Abstract

Directional solidification experiments on hypoperitectic Cu–Sn alloys have been performed at very low velocity in a high thermal gradient to ensure planar front growth of both phases. The diameter of the sample has been reduced to 500 μm to strongly reduce convection. Lamellar and fibrous peritectic cooperative growth of the primary α- and peritectic β-phases has been observed on length spanning several millimeters. For the first time in a high solidification interval peritectic alloy, a quenched interface of both phases in contact with the liquid has been obtained. An unexpectedly high volume fraction of the primary phase, which furthermore fluctuates over time, has been observed. This is attributed to the transient state of the (α + β) growth front to a steady state and the associated evolution of the large diffusion layer ahead of the solid–liquid interface.

Keywords: Peritectic solidification; Directional solidification; Copper alloys; Cooperative growth

1. Introduction

Peritectic phase diagrams are frequently observed in many commercially important alloys, such as steels (Fe–C, Fe–Ni), brasses (Cu–Zn), bronzes (Cu–Sn) and some aluminium alloys (Al–Ti). In such systems, the primary α-phase reacts upon cooling with the liquid phase to yield the peritectic β-phase at the peritectic temperature T_{per}. In the hypoperitectic region of peritectic metallic systems, various new microstructures have been revealed during directional solidification experiments at low growth rates, i.e. where both α- and β-phases would grow independently as planar fronts [1–8]: (i) discrete bands of α- and β-phases; (ii) partial bands or islands of one phase in the matrix of the other phase; and (iii) cooperative growth of both phases with a planar solid–liquid interface. Up to now, cooperative growth of the two phases has only been observed in peritectic alloys with a small solidification interval (a few kelvin) [8–10]. Kohler et al. [11,12] were able to produce recently such microstructure in hypoperitectic Cu–Sn alloys with a high freezing range of ~100 K, but with considerable solutal convection in their samples. In the present work, directional solidification experiments are carried out on Cu–21 wt.% Sn alloys at a high G_l/V_p ratio, but with a diameter of the samples reduced to 500 μm, which strongly limits convection.

2. Theoretical background

The microstructures found in the hypoperitectic region at low growth rates result from the specific shape of the peritectic phase diagrams (Fig. 1). Consider a hypoperitectic alloy of nominal composition C_0 directionally solidified at a low velocity that guarantees planar front growth for both phases. During the initial transient, the solute rejected in the liquid by the primary phase builds up a solute boundary layer. Accordingly, the temperature of the interface decreases from $T^{\alpha}_{liq}(C_0)$ to the steady-state solidus temperature $T^{\alpha}_{sol}(C_0) = T^{\alpha}_{liq}(C_0/k_{\alpha})$, located below T_{per}, where k_{α} is the corresponding partition coefficient. When the composition of the liquid at the α–liquid interface, $C^{*\alpha}_l$, exceeds the

* Corresponding author. Tel.: +41 216933943.
E-mail address: jonas.valloton@epfl.ch (J. Valloton).

1359-6454/$36.00
http://dx.doi.org/10.1016/j.actamat.2012.03.030

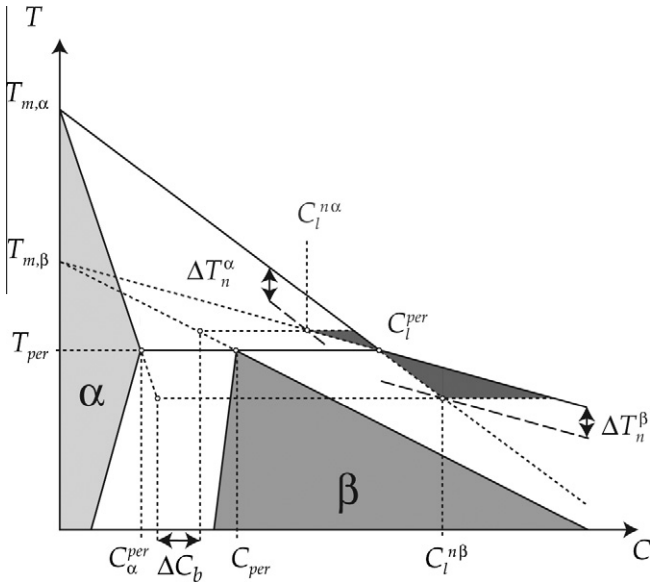

Fig. 1. Schematic peritectic phase diagram with the banding mechanism developed by Trivedi [1] for initial alloy compositions situated in the banding window ΔC_b, for k_α and $k_\beta < 1$. ΔT_n^α and ΔT_n^β correspond to the nucleation undercoolings for the α- and β-phases, respectively.

liquid composition at the peritectic temperature $C_l^{per} = C_l(T_{per})$, it becomes undercooled with respect to the β-phase. Thus, β can nucleate heterogeneously if its corresponding nucleation undercooling, ΔT_n^β, is reached. Once the peritectic phase has nucleated, growth competition between the two phases is initiated. Assuming infinitely fast lateral spreading of the newly nucleated phase (or, equivalently, infinitely high nucleation density) [1], the β-phase blocks any further growth of the primary α-phase. As the solute boundary layer decreases, i.e. less solute rejected by the β-phase since $k_\beta > k_\alpha$, the temperature of the interface increases and tends to reach $T_{sol}^\beta(C_0) = T_{liq}^\beta(C_0/k_\beta)$, the steady-state temperature of the β-planar interface. However, for alloy compositions in the hypoperitectic range, $T_{sol}^\beta(C_0)$ is located above T_{per}. Then, as the composition $C_l^{*\beta}$ at the β–liquid interface falls below C_l^{per}, the liquid becomes now undercooled with respect to the α-phase. Similarly, when the undercooling reaches a critical value, ΔT_n^α, the primary phase can nucleate and cover the peritectic phase and this banding cycle can then start over again. Knowing the nucleation undercoolings of the two phases, a banding window for stable cycles, ΔC_b, can be determined, as shown in Fig. 1 [1]. For hypoperitectic compositions below this range, the primary phase is at a steady state before ΔT_n^β is reached, whereas alloys with a composition above ΔC_b exhibit a single α-to-β transition, with the peritectic phase reaching a steady state before any new nucleation of the primary phase.

In order to explain the formation of islands rather than bands, the above approximation of infinitely fast lateral spreading must be relaxed. Indeed, while the newly nucleated phase spreads laterally, the first phase continues to grow along the thermal gradient and, depending on the growth conditions, it might engulf the forming band. Using a multi-phase field, Lo et al. [7] showed that island growth occurs for internuclei distances below a critical distance, while band growth is expected above this distance.

Finally, another interesting microstructure that can form in peritectic alloys at low growth rate is the simultaneous growth of α- and β-lamellae. Although similar to eutectic coupled growth, the α- and β-lamellae of peritectic alloys both reject solute elements ahead of the interface. Predicted in 1959 by Chalmers [13], coupled growth was first observed in 1994 in Ni–Al by Lee and Verhoeven [9], and then in Fe–Ni by Vandyoussefi et al. [10] and Dobler et al. [8]. Directional solidification experiments and multi-phase field simulations [7,8,14,15] showed that lamellar structures can start growing from islands, providing the distance separating the islands falls within a range of stable lamellar spacings [7].

The observations of bands, islands and cooperative lamellar growth in peritectics has been limited up to now to small solidification interval alloys, typically with $\Delta T_0 = \left(T_{liq}^\alpha(C_0) - T_{per}\right) \simeq 5$ K. Recently, Kohler et al. [11,12] investigated peritectic solidification in the Cu–Sn system, an alloy with a solidification interval ΔT_0 nearly 20 times that of Fe–Ni in the hypoperitectic region (around 100 K). Using a liquid metal cooling (LMC) Bridgman solidification setup with quench, these authors observed all three of the peritectic microstructures discussed above – lamellae, bands and islands – but their sample showed appreciable convection. Using synchrotron-based X-ray microtomography, Rappaz et al. [16] confirmed a new growth mechanism of bands: α- and β-phases can be totally interconnected in three dimensions and bands (or islands) can result from an overlay mechanism, rather than from subsequent nucleation events. When the lateral growth of a new layer is too fast, an instability can lead to the formation of a lamellar structure as for eutectic alloys.

3. Experimental method

Many Cu–Sn phase diagrams are available in the literature, and most often these diagrams differ slightly from each other. Notably, the reported peritectic temperature T_{per} varies from 795.7 to 798 °C, and the equilibrium concentrations C_α^{per}, C_{per} and C_l^{per} are not defined accurately. The most widely used Cu–Sn phase diagram, shown in Fig. 2, comes from the Metals Handbook, Metallography, Structures and Phase Diagrams from the American Society for Metals (ASM) [17]. Recently, Liu et al. [18] reinvestigated this phase diagram (see the enlargement in Fig. 2) and showed that the $\beta - \gamma$ domain is actually a succession of second-order ordering transitions and that the $\beta \rightarrow \alpha + \gamma$ and $\beta + \text{liquid} \rightarrow \gamma$ invariant reactions are non-existent. β and γ are thus considered to be one and the same phase.

In practice, two solid-state transformations within the β-phase can complicate the analysis of the resulting micro-

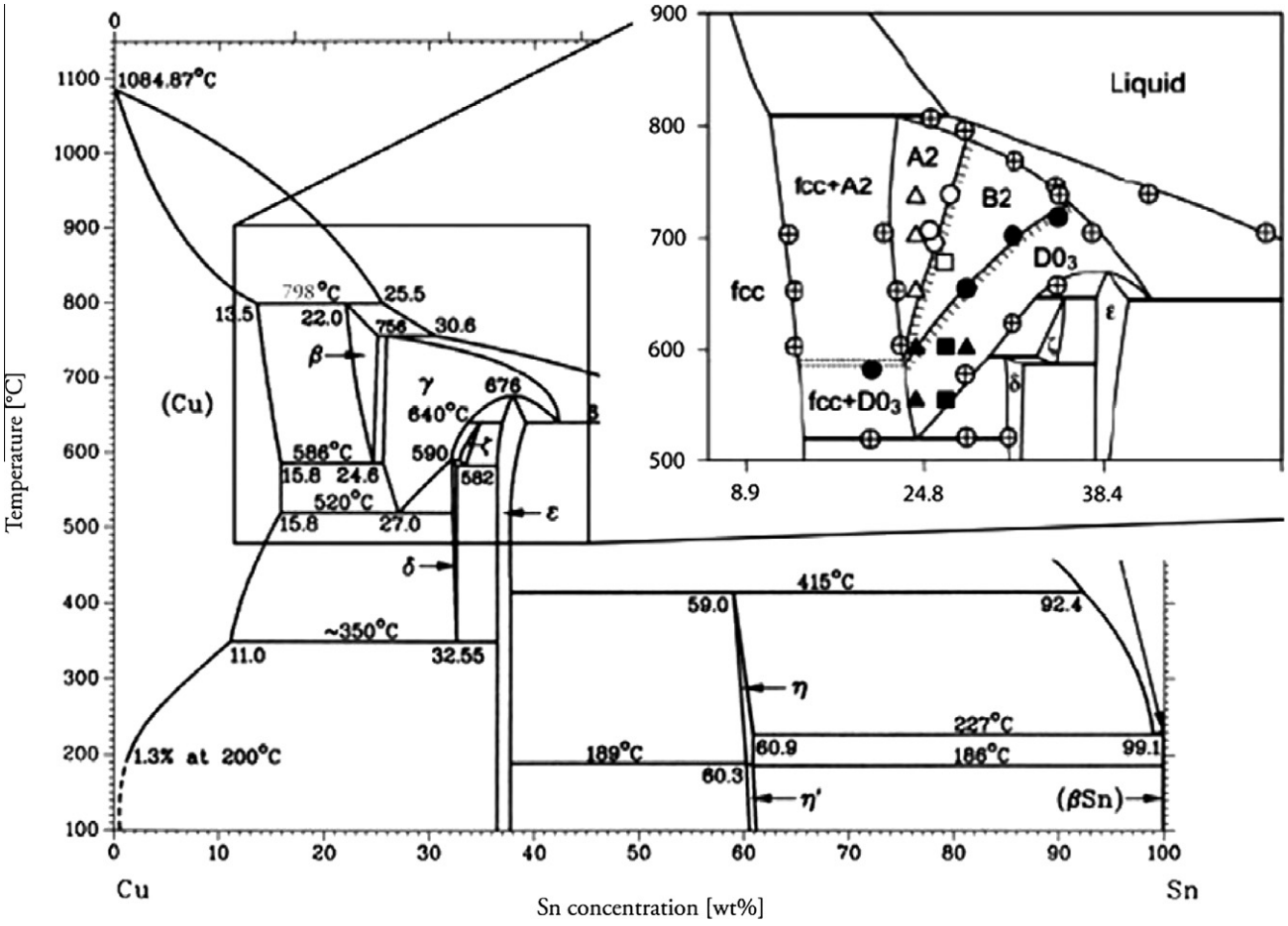

Fig. 2. ASM Cu–Sn phase diagram with an enlargement of the β- and γ-phases regions recently reinvestigated by Liu et al. [18].

structure after quench: (i) a partial decomposition into an acicular martensitic microstructure for compositions between about 22 and 24 wt.% Sn, corresponding to a temperature of the β-phase at the time of quench between 798 and 620 °C, which prevents the indexation of the peritectic phase during electron backscattered diffraction (EBSD) analysis; (ii) at 520 °C, a eutectoid decomposition of the peritectic phase occurs, $\beta \rightarrow \alpha + \delta$, which also hinders EBSD indexation if the resulting microstructure is very fine.

The Bridgman furnace used in this work has been already described in [8,11]. It is composed of three parts: (i) a closed chamber containing a cylindrical molybdenum susceptor surrounded by an induction coil that controls heating; (ii) a water-cooled Ga–25 wt.% In–13 wt.% Sn LMC bath for efficient heat extraction ($T_{LMC} \approx 20\ ^{\circ}C$); and (iii) an adiabatic zone in between. A vacuum pump and a gas inlet are connected to the mounting head to evacuate and purge the crucibles containing the samples to be solidified.

Cu–21 wt.% Sn alloys are cast from Cu and Sn of 99.99% purity in a vacuum induction furnace. Wire electrodischarge machining is then used to machine the cast samples into tubes (OD 3.95 mm, ID 2.2 mm, length 80 mm). A double-bore alumina capillary (OD 2 mm, ID 500 μm, length 100 mm) is inserted into the 80 mm Cu–21 wt.% Sn tube and two centering boron nitride rings are subsequently affixed to the ceramic (Fig. 3). The bottom of the capillary is blocked with alumina paste and an additional 40 mm CuSn tube is added at the top. The whole set-up is finally inserted in an OD 7 mm, ID 4 mm alumina crucible and mounted in the Bridgman furnace.

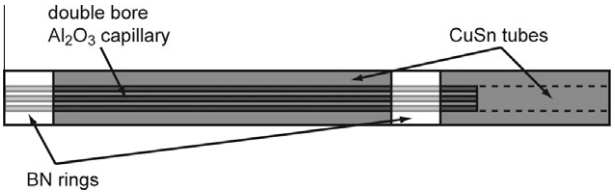

Fig. 3. Sample experimental setup. A 100 mm long double-bore alumina capillary (OD 2 mm, ID 0.5 mm) is inserted into two 80 mm and 40 mm long Cu–Sn tubes, with two boron nitride centering rings.

Prior to heating, the furnace chamber and the crucible are evacuated and purged with Ar twice. After an initial controlled heating up to 750 °C with the sample fully inserted in the susceptor, the crucible is evacuated and purged with Ar three times and evacuated one last time. The crucible is then moved to its uppermost position and the temperature is increased to 1100 °C. Directional remelt-

ing of the sample from the upper position is then started on the descent at 1 mm min^{-1} until the whole sample is again fully inserted in the susceptor. An overpressure of about 3 bars of argon is applied in the crucible in order to infiltrate the two 0.5 mm bores of the alumina capillary with liquid CuSn. The crucible is thereafter lowered at 1 mm min^{-1} until it is immersed 15 mm in the LMC bath. To establish a high thermal gradient of $G_l \approx 20$ K mm^{-1}, the susceptor temperature is further increased to 1500 °C, followed by a thermal arrest of 45 min for thermal stabilization. Following these steps, directional solidification is carried out at a pulling velocity $V_p = 0.58$ μm s^{-1} (ensuring planar front growth for both phases) for a processing length of 10–40 mm before the quench in the LMC bath.

The quenched samples are then taken out of the alumina capillary and mounted in a conductive resin. Rough polishing is first carried out using silicon carbide papers, followed by fine polishing with 1 and 0.25 μm diamond particles on soft cloths. Finally, vibrating polishing is carried out on a soft cloth with a colloidal solution. The microstructure are then observed by optical and scanning electron microscopy (SEM). The composition is measured with energy-dispersive X-ray spectroscopy (EDX) or wavelength-dispersive X-ray spectroscopy (WDS). For EBSD analysis, another vibrating polishing step is necessary to remove the small work-hardened layer at the surface of the sample. For this, 2 vol.% NH_4 and 2 vol.% H_2O_2 are added to the colloidal suspension.

4. Results and discussion

4.1. General features of the specimens

Directional solidification experiments on Cu–21 wt.% Sn alloys at $V_p = 0.58$ μm s^{-1} yielded many different microstructures due to the growth competition between the primary and peritectic phases. Figs. 4 and 5 show the first and second parts of solidification of a sample processed for 40.

The onset of the α-planar front can be clearly seen on the left side of Fig. 4. The (α + β) zone visible at the very beginning of the micrograph corresponds to the part of the specimen that solidifies when the crucible is immersed in the LMC bath at 1 mm min^{-1} prior to the start of the low-speed solidification run. Thus, a concentration profile is initially present ahead of the solid–liquid interface. However, one-dimensional simulations of the initial transient [19] show that it does not significantly affect the transient planar front growth of the primary phase as the low-speed directional solidification proceeds. After about 2.5 mm, nucleation of the β-phase is observed and growth competition is initiated. The latter results in a tilted lamellar structure spanning over 7 mm, similar to that of eutectics. This cooperative growth mode will be discussed further later.

As can be seen in Fig. 4, the EBSD analysis reveals that the primary phase is initially made of three different grains (in pink, red and purple on the false color map), with the purple one taking over the two others after 3–4 mm of solidification. However, careful observation of the pole figure indicates a twinning relationship between the pink and purple grains. This suggests that the planar front growth started with two different grains, red and pink, with the latter winning the competition after twinning. Note that the red grain has the same crystallographic orientation as the existing α-phase in the (α + β) zone present at the beginning of the experiment. The onset of solidification then saw both the continued growth of a pre-existing grain and the nucleation of at least one new grain at the solid–liquid interface. Note that, due to the eutectoid transformation and the small size of the lamellae, the β/δ-phase in the quenched (α + β) region could not be indexed.

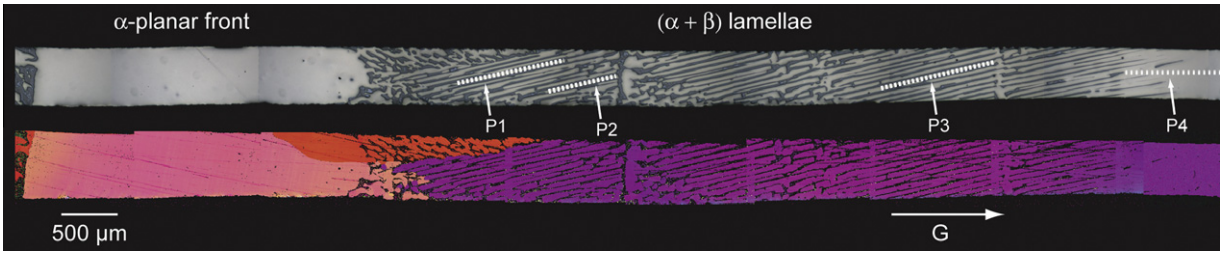

Fig. 4. Optical micrography (top) and EBSD analysis (bottom) of the first part of a Cu–21 wt.% Sn sample solidified at $V_p = 0.58$ μm s^{-1} in a gradient $G_l = 20$ K mm^{-1}. The lines P1–P4 correspond to the positions of the composition profiles shown in Figs. 8 and 9.

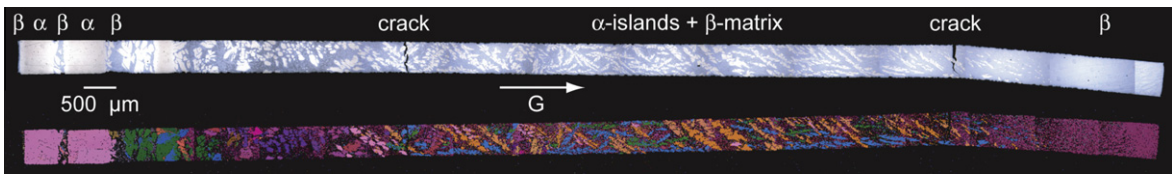

Fig. 5. Optical micrography (top) and EBSD analysis (bottom) of the second part of the Cu–21 wt.% Sn sample shown in Fig. 4. Note the change of scale compared to Fig. 4 and the small bending/crack of the specimen on the right, which was induced during polishing.

After the cooperative (α + β) growth mode in Fig. 4, the peritectic phase disappears and the primary phase grows alone for 4 mm (not shown entirely in Fig. 4). Subsequently (Fig. 5), bands of α and β alternate over ~ 2.5 mm. Note a thin band of β separating two larger bands of α on the left of Fig. 5. The remaining of the structure is then made of islands (or regions) of the primary phase in a matrix of the peritectic phase. Two small cracks are visible in this figure; these are due to the manipulation of the very small specimens. However, due to wetting problems of Cu–Sn alloys on the alumina crucible, a discontinuity of the sample (bubble) was present just after this portion of the specimen. As for a final transient, this induced a solute enrichment of the right part of the specimen shown in Fig. 5 (keep in mind that the solute layer is 6–7 mm). As a result, only the peritectic phase remains. At the time of the quench, the whole sample was below 520 °C and so the β-phase region actually transformed into a fine α + δ eutectoid.

The EBSD reconstructed microstructure of the specimen part shown in Fig. 5 indicates that the two bands of α on the left correspond to the primary grain in the first part of the specimen (Fig. 4). This observation confirms the overlay growth mechanism evidenced by Kohler et al. [11,12,16]: a new band of α does not necessarily needs to nucleate ahead of β, even in a small capillary, but can start from another α part of the specimen which is not in the section plane. After these bands, the various colors of the numerous α-grains present in the matrix of β (which has transformed into an (α + δ) eutectoid) reveal that they have different crystallographic orientations. This implies renucleation of the primary phase at the β–liquid interface, as described by Trivedi in a purely diffusive growth regime [1]. On this part of the sample, the β-phase could be indexed from the δ-phase of the eutectoid and appears to be a single grain whose $\langle 1\,0\,0\rangle_\beta$ directions are shown in the pole figure of Fig. 6a.

The eutectoid δ-phase is an intermetallic cubic ordered superstructure of composition ~$Cu_{41}Sn_{11}$. Its lattice contains 412 atoms and its parameter is $a = 17.98$ Å [20,21]. Careful observation of the eutectoid reveals that all the pro-eutectoid α-grains are surrounded by a 5–10 μm thick layer of δ-phase (Fig. 7). This indicates that, as the solid state transformation occurs, the δ-phase nucleates at the α − β interface and grows in the β-phase, thus depleting

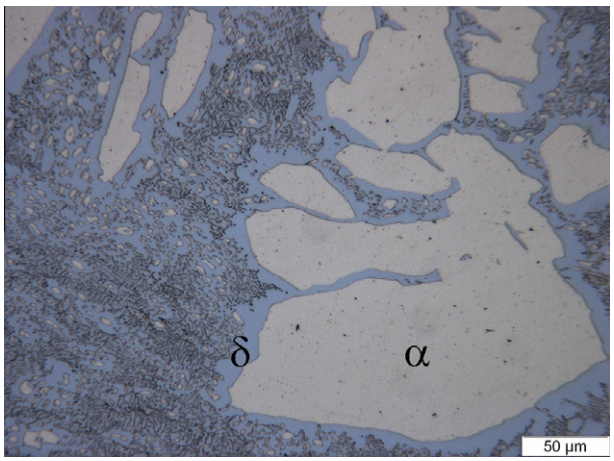

Fig. 7. Enlargement of α-islands within the (α + δ) eutectoid.

the latter in solute. Consequently, nucleation of the α-phase in the eutectoid starts at the β–δ interface and then into the β-bulk. As the δ-phase nucleates multiple times around different α-grains, it is unlikely that all the nuclei should have the same orientation. Thus, observing only one orientation for the δ-phase, it appears that it retains the orientation of its mother β-phase and that this latter was constituted of a single grain.

Looking at the $\langle 1\,1\,0\rangle_\alpha$ pole figure for the primary phase domains present in the (α + β) region (Fig. 6b), one can again see numerous different orientations. However, these $\langle 1\,1\,0\rangle_\alpha$ poles are not distributed randomly but show a very well-defined symmetry, indicating a possible orientation relationship with the single β-grain (Fig. 6a). Indeed, all the face-centered cubic (fcc) α-grains have a so-called Kurdjumov–Sachs (K–S) relationship with the peritectic body-centered cubic (bcc) β- (now δ-) phase, i.e. $\{1\,1\,1\}_\alpha // \{1\,1\,0\}_\beta$ and $\langle 1\,1\,0\rangle_\alpha // \langle 1\,1\,1\rangle_\beta$. For one specifically oriented bcc grain of the peritectic phase, there are 24 different ways of accommodating the fcc grains with the K–S relationship. All the possible orientations for fcc grains on a bcc grain with $\langle 1\,0\,1\rangle$ directions aligned with the axis of the pole figure can be calculated and have been plotted in Fig. 6c: with a small rotation (equivalent to the misalignment of the $\langle 1\,0\,1\rangle_\beta$ directions with the axis of the pole figure), it closely matches the experimental pole figure obtained by EBSD. This also supports the fact that the eutectoid δ-phase has the same crystallographic orientation as the β-phase since

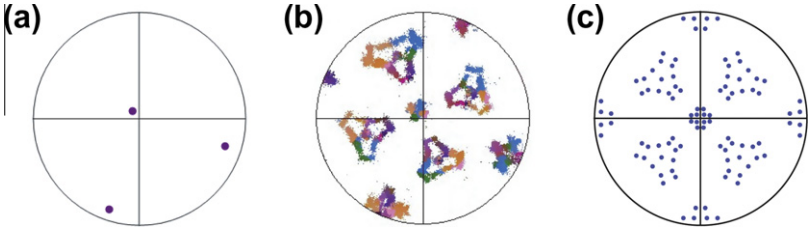

Fig. 6. (a) EBSD $\langle 1\,0\,0\rangle$ pole figure for the β-phase of Fig. 5. (b) EBSD $\langle 1\,1\,0\rangle$ pole figure for the α-phase of Fig. 5. (c) Computed $\langle 1\,1\,0\rangle$ pole figure with all possible Kurdjumov–Sachs orientations of fcc grains on a single bcc grain, having $\langle 1\,0\,0\rangle$ directions aligned with the axis of the figure.

the specific K–S orientations of the α-grains originated when they nucleated in contact with the peritectic phase but the orientation of the δ-phase also matches the K–S relationship.

4.2. Cooperative growth of (α + β)

We now return to the cooperative growth structure seen in Fig. 4. Local compositions have been measured with EDX in the α-lamellae along the lines P1, P2 and P3 shown in this figure. As can be seen in Fig. 8, the composition within each lamella is fairly constant. In order to put into relation these measured compositions with the phase diagram (Fig. 2), we must account for the peritectic transformation that occurred between the temperature at which these lamellae formed ($T_{per} = 798$ °C) and the temperature at which they were quenched. Considering that the eutectoid structure seen in Fig. 5 has already formed (i.e. temperature below 520 °C at the time of the quench), the P1, P2 and P3 locations are already nearly at the temperature of the liquid metal cooling bath. The time t_d available for solid-state diffusion is equal to $\Delta T/(G_l V_p)$, where $G_l = 20$ K mm^{-1}, $V_p = 0.58$ μm s^{-1} and ΔT is the temperature difference between T_{per} (the temperature at which the lamellae formed) and room temperature. For the CuSn peritectic system, Oikawa and Hosoi [22] showed that the diffusion coefficient D_s in the α-phase can be approximated by the following equation:

$$D_s(T) = 1.82 \times 10^{-5} \exp\left(-\frac{1.56 \times 10^5}{RT}\right) \mathrm{m^2\ s^{-1}}$$

The Fourier number can then be integrated:

$$F_o = \int_0^{t_d} \frac{D_s(T(t))}{d^2} dt$$

The "longitudinal" Fourier number associated with the length of the measured composition profiles ($d = 600$–1000 μm) is found to be smaller than 0.01. This means that there is almost no Sn diffusion at the scale of the length of the lamellae and therefore the nearly constant composition profiles measured along P1, P2 and P3 mean that the composition was also constant during growth of the lamellae.

Considering now the spacing of the lamellae (about 30–40 μm), the integrated "transverse" Fourier number is about 400 times larger than the longitudinal one, i.e. nearly complete mixing can be considered between the α- (or β-) phase in the transverse direction. This means that the composition of α and β must follow the solvus lines, which have a negative slope (see Fig. 2), at least until solid-state diffusion becomes negligible. Since $D_s < 5e-16$ m^2 s^{-1} below the $\beta \rightarrow \alpha + \delta$ eutectoid (520 °C), almost no back-diffusion occurs below this temperature. Thus, we can take the maximum solubility limit of Sn in the α-phase (15.8 wt.% at the eutectoid temperature) as a reference for the comparison with the compositions measured at P1, P2 and P3. As can be seen, these compositions are slightly higher. This finding is in agreement with that of Kohler et al. [11,12], who also found higher compositions for the solvus from their lamellar structure.

Fig. 9 shows the composition profile at the transition from the cooperative growth of α- and β-lamellae to a pure α-planar front (line P4 of Fig. 4). Note that the profile extends further in the α-phase than what is shown on the micrography. A sharp decrease of the Sn composition is observed when cooperative growth of the two phases stops: C_α decreases over a distance of about 300 μm from 17 wt.%, i.e. the steady value of cooperative growth measured along P1, P2 and P3 (Fig. 8), to 14.5 wt.%. It then increases slowly in a transient regime up to the point where the increase is faster just before new bands of β form (Fig. 5). The reason why cooperative growth of α and β stops is not yet clear: it could be due to solutal convection, as in the experiments of Kohler et al. [11,12], but normally convection is considerably reduced in the small capillaries used in the present experiment. Furthermore, convection should increase the Sn concentration of the liquid and favor formation of β. The most probable explanation is a conjunction of several phenomena: (i) variations of the solute boundary layer, from $\Omega_\alpha D_l/V_p$ when only the α-phase

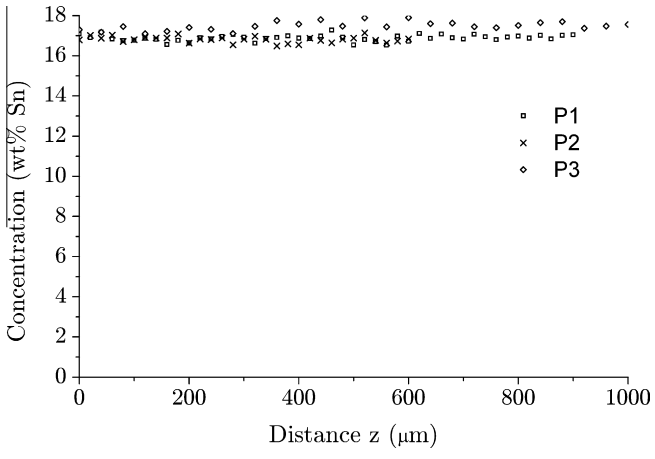

Fig. 8. EDX local composition measurements in the α-lamellae along the lines P1, P2 and P3 of Fig. 4.

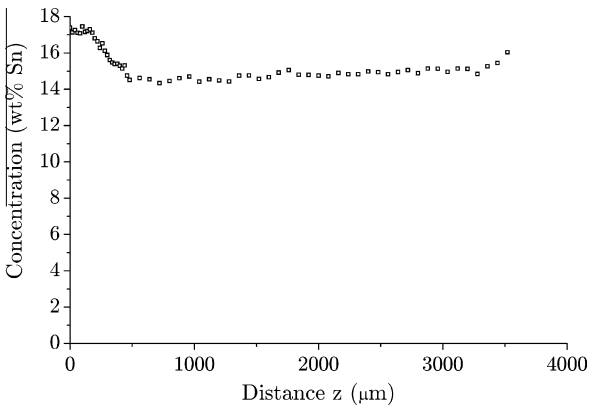

Fig. 9. EDX local composition measurements in the α-phase over the transition from lamellae to single α growth (line P4 in Fig. 4).

grows in a transient regime (Ω_α is the supersaturation) to D_l/V_p during steady-state cooperative growth; (ii) variations of the partitioning coefficient of the interface, from k_α when only the α-phase is growing to ($k_\alpha g_\alpha + k_\beta g_\beta$) when both phases grow (g_α and g_β are the respective volume fractions of solid).

In any case, once α grows as a single phase, there is no solute redistribution in the solid upon cooling unlike in the two-phased α + β regions; the α-phase keeps the composition it had during growth. As will be shown later, the composition of 14.5 wt.% reported in Fig. 9 after coupled growth has stopped ($z \approx 500$ μm) is close to the composition of the primary phase measured at a quenched cooperative growth interface (Fig. 11). Therefore, the distance of transition seen in Fig. 9 measures the diffusion distance during further cooling between a region where only α is present (and essentially keeps its solidified composition) and a region where both α and β coexist (and where C_α has to follow the α-solvus if equilibrium is assumed up to about the eutectoid temperature).

To further analyze this sample, X-ray microtomography experiments were carried out at the TOMCAT beamline of the Swiss Light Source (Paul Scherrer Institute, Villigen, Switzerland). As both Cu and Sn are strong X-ray absorbers, the specimen has been trimmed down to a squarish section of $\sim 300 \times 300\ \mu m^2$ in order to obtain enough transmission. The energy of the X-ray beam was 40 keV, the voxel size was 0.74 μm and the specimen-to-screen distance was 2 mm.

Fig. 10 (left) shows a reconstructed slice perpendicular to the thermal gradient G_l. The image is shown in reverse contrast, with the α-phase appearing in dark gray since it is leaner in Sn while the β-phase appears brighter. The structure is quite regular, with a thickness of the α-lamellae $\lambda_\alpha \approx 25$–30 μm and of the β-lamellae $\lambda_{beta} \approx 6$–7 μm. In this image, the volume fraction of the primary phase is found to be $g_\alpha \approx 80\%$. (Note that the value of g_α is actually higher as the β-lamellae decomposed into an α + δ eutectoid after solidification. However, the newly nucleated α-grains are numerous and small (~1–3 μm, Fig. 7), and are thus not visible at the resolution of tomography.) The density of the two phases being almost equal (±1%), the volume fraction corresponds to the mass fraction f_α. The experimental fraction deduced by the X-ray microtomography is higher than what is expected at equilibrium. According to the lever rule, f_α is about 12% at the peritectic temperature when cooperative growth occurs, and 69% at the eutectoid temperature when solid-state diffusion is assumed to become negligible.

The right part of Fig. 10 shows a three-dimensional (3-D) segmented view of the β-phase from a subsection of the specimen in Fig. 4. It can be seen that the orientation of the lamellae in three dimensions remains the same although their growth is not fully stable. Along the solidification sequence, some of the β-lamellae briefly bridge together or even form islands/bands before growing again as lamellae. Fig. 10 also shows that the peritectic phase is continuous, and so is the primary phase, as already demonstrated by the EBSD map (Fig. 4). The growth competition between the two phases is clearly a 3-D process.

Fig. 11 (right) shows an α − β interface growing into the liquid at the time of the quench for another Cu–21 wt.% Sn specimen solidified under identical conditions. A transverse cut located 350 μm below the quenched interface is shown on the left. Note that a discontinuity was present in the capillary and thus solidification of this sample started out from liquid with no solid present beforehand for a processing length of ~10 mm. The quenched interface clearly exhibits a cooperative growth of α- and β-fibers. To the authors' knowledge, this is the first time that both primary and peritectic phases have been shown to be present at the quenched interface of a high solidification interval peritectic alloy solidified at low speed. The presence of both solid phases in contact with the liquid means that the solidification front has to be at, or close to, the peritectic tempera-

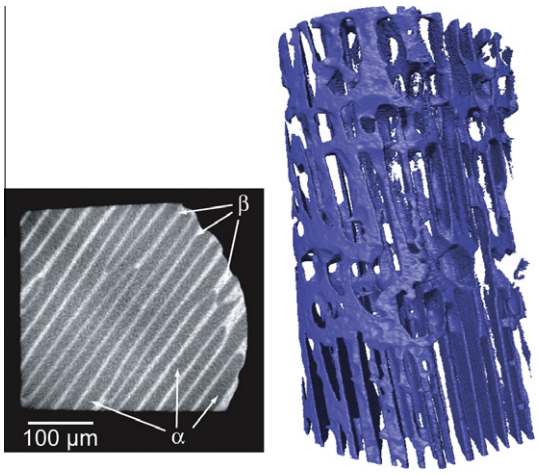

Fig. 10. X-ray microtomography in the lamellar cooperative growth of the specimen shown in Fig. 4, i.e. at a temperature much below the eutectoid temperature at the time of the quench. Left: reconstructed slice perpendicular to the thermal gradient G_l. Right: 3-D segmented view of the β-phase. The thermal gradient G_l is vertical and up.

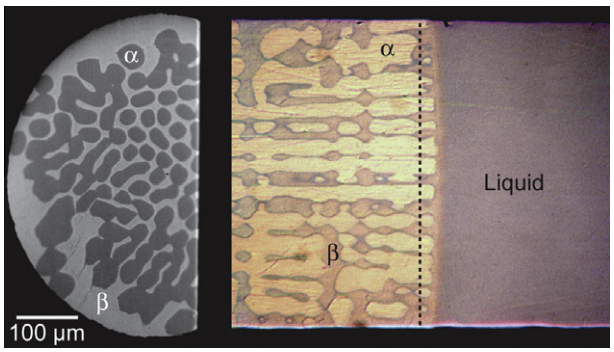

Fig. 11. SEM transverse cut (left) and optical micrography (right) of a Cu–21 wt.% Sn sample solidified at $V_p = 0.58\ \mu m\ s^{-1}$ in a gradient $G_l = 20\ K\ mm^{-1}$, showing a quenched α–β interface that was growing cooperatively into the liquid.

ture since the curvature undercooling is very small considering the lamellae spacing, but is not necessarily strictly isothermal. The peritectic phase should be slightly ahead of the primary phase, as predicted by phase field computations [7,12]. In fact, a thin layer of the β-phase can be seen just ahead of the cooperative front; it probably formed during the quench, and could indicate that the peritectic phase grows slightly ahead of the primary phase during solidification.

Microprobe composition measurements have been performed close to the quenched interface along the dashed line in Fig. 11. The results (Fig. 12) show a constant composition in the primary phase (~14 wt.%), very close to the one given by the phase diagram (13.5 wt.%) and to the value measured along the profile P4 when only the α-phase is growing near the peritectic temperature (Fig. 9). The composition in the peritectic phase is systematically higher than the value given by the phase diagram (Fig. 2). Note that a very thin Sn-rich layer (~2 μm) forms around the primary phase during the quench, thus explaining higher concentrations at both extremities of the α-fibers. However, the mean composition in the peritectic phase (~24.5 wt.% Sn) is 2.5 wt.% higher than the theoretical value. On the other hand, the transverse cut of Fig. 11, which is just below the peritectic temperature at the time of the quench, shows a fraction of α $g_\alpha \approx 60\%$, which is much higher than that predicted from the lever rule at the peritectic temperature. Indeed, the theoretical fraction g_α for an initial composition of 21 wt.% Sn should be about 12% at steady state, i.e. a value five times less than the experimental one. With the compositions previously measured, the mean composition of the cut would be ~18.4 wt.% Sn, i.e. 2.6 wt.% less than the initial composition of the alloy. This means that a steady-state solidification planar front of cooperative growth, i.e. with a diffusion layer ahead of the front equal to D_l/V_p, was not achieved and that the solute content of the large diffusion layer was still varying. This point will be addressed in a forthcoming theoretical study.

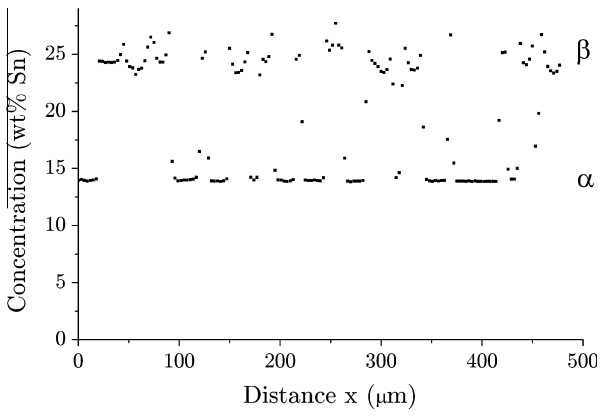

Fig. 12. WDS local composition measurements along the dashed line of Fig. 11 in the quenched cooperative zone.

5. Conclusion

Both lamellar and fibrous peritectic cooperative growths have been observed in the peritectic Cu–Sn system in a diffusive regime. For the first time, a quenched α + β front has been obtained in a high solidification interval peritectic alloy. Hitherto, such morphologies were only observed in peritectic systems for which the freezing range of the primary phase is of only a few kelvins. Though the peritectic phase seems to be growing ahead of the primary phase, it is still unclear whether the cooperative front is isothermal or not, or if it is located above [2], below [9] or across [11,12] T_{per}. Both morphologies see instabilities during growth, such as bridging of the lamellae and oscillations along the fibers. An unexpectedly high volume fraction of the primary phase, which varies over time, has been observed far from and close to the quenched interface. These observations show that the cooperative growth front never reached a steady state. This is thought to be due to variations over time of the large solute layer ahead of the growth front and of the partitioning coefficient of the interface, and to the continuous growth competition between the two phases. Experimental runs with longer processing lengths will be carried out in order to possibly obtain a cooperative front at steady state. A simple numerical model is also currently being developed to see the evolution of the diffusion layer of the cooperative α + β front once the peritectic phase nucleates. Finally, a systematic Kurdjumov–Sachs orientation relationship has been found between the primary fcc phase and the peritectic bcc phase, which facilitates multiple renucleation of the primary phase on the peritectic phase.

Acknowledgements

The authors thank Dr. E. Boehm-Courjault for the electron microscopy analyses performed at the CIME, Interdisciplinary Centre for Electron Microscopy (Ecole Polytechnique Fédérale de Lausanne, Switzerland), as well as Dr. A.B. Phillion and Dr. J. Fife for the tomography analyses carried out at the TOMCAT beamline of the Swiss Light Source (Paul Scherrer Institute, Villigen, Switzerland). Financial support from the Swiss National Science Foundation under Grants ♯200020-121598 and ♯ 200020-132848 is also gratefully acknowledged.

References

[1] Trivedi R. Met Mater Trans 1995;26A:1583.
[2] Kerr H, Kurz W. Int Mater Rev 1996;41:129.
[3] Trivedi R, Karma A, Lo T, Park J, Plapp M. In: Solidification microstructures, Proc. 2nd Workshop Zermatt. Zermatt, Switzerland, 1998.
[4] Hunziker O, Vandyoussefi M, Kurz W. Acta Mater 1998;46:6325.
[5] Karma A, Rappel W, Fuh B, Trivedi R. Met Mater Trans 1998;29A:1457.
[6] Trivedi R, Park J. J Cryst Growth 2002;235:572.

[7] Lo T, Dobler S, Plapp M, Karma A, Kurz W. Acta Mater 2003;51:599.
[8] Dobler S, Lo T, Plapp M, Karma A, Kurz W. Acta Mater 2004;52:2795.
[9] Lee J, Verhoeven J. J Cryst Growth 1994;144:353.
[10] Vandyoussefi M, Kerr H, Kurz W. Acta Mater 2000;48:2297.
[11] Kohler F, Germond L, Wagnière JD, Rappaz M. Acta Mater 2009;57:56.
[12] Kohler F. Peritectic solidification of Cu–Sn alloys: microstructure competition at low speed. PhD thesis, ♯ 4037, Ecole Polytechnique Fédérale de Lausanne, Switzerland; 2008.
[13] Chalmers B. Physical metallurgy. New York: Wiley; 1959.
[14] Dobler S, Kurz W. Z Metall 2004;95:592.
[15] Lo T, Karma A, Plapp M. Phys Rev E 2001;63:031504.
[16] Rappaz M, Kohler F, Valloton J, Phillion A, Stampanoni M. Met Mater Trans 2010;41A:563.
[17] American Society for Metals (Ed.). Metals Handbook, Metallography, Structures and Phase Diagrams. Metals Park, 1973.
[18] Liu X, Wang C, Ohnuma I, Kainuma R, Ishida K. Met Mater Trans 2004;35A:1641.
[19] Sanglard R. Calculation of the initial transient and estimation of the liquid diffusion coefficient during directional solidification of a Cu–10 wt.%Sn alloy. Master's thesis, Ecole Polytechnique Fédérale de Lausanne, Switzerland; 2011.
[20] Arnberg L, Jonsson A, Westman S. Acta Chem Scand 1976;30A:187.
[21] Booth M, Brandon J, Brizard R, Chieh C, Pearson W. Acta Crystallogr 1977;33B:30.
[22] Oikawa H, Hosoi A. Scripta Met 1975;9:823.